Letter | Editors' Suggestion

Observation and spectroscopy of the proton-unbound nucleus ^{21}Al

D. Kostyleva,[1] X.-D. Xu,[2,1,*] I. Mukha,[1] L. Acosta,[3,4] M. Bajzek,[1,5,6] E. Casarejos,[7] A. A. Ciemny,[8] D. Cortina-Gil,[9] W. Dominik,[8] J. A. Dueñas,[10] J. M. Espino,[11] A. Estradé,[12,13] F. Farinon,[1] A. Fomichev,[14] H. Geissel,[1,5,†] J. Gómez-Camacho,[11] A. Gorshkov,[14] L. V. Grigorenko,[14,15,16] Z. Janas,[8] G. Kamiński,[17,14] O. Kiselev,[1] R. Knöbel,[1,5] A. A. Korsheninnikov,[16] S. Krupko,[14] M. Kuich,[18,8] N. Kurz,[1] Yu. A. Litvinov,[1] G. Marquinez-Durán,[19] I. Martel,[20] C. Mazzocchi,[8] E. Yu. Nikolskii,[14,16] C. Nociforo,[1] A. K. Ordúz,[21] M. Pfützner,[8,1] S. Pietri,[1] M. Pomorski,[8] A. Prochazka,[1] C. Rodríguez-Tajes,[9] S. Rymzhanova,[14] A. M. Sánchez-Benítez,[22] C. Scheidenberger,[1,5,23] H. Simon,[1] B. Sitar,[24] R. Slepnev,[14] M. Stanoiu,[25] P. Strmen,[24,†] K. Sümmerer,[1] I. Szarka,[24] M. Takechi,[1] Y. K. Tanaka,[26,1] H. Weick,[1] J. S. Winfield,[1,†] P. J. Woods,[12] and M. V. Zhukov[27]

[1]*GSI Helmholtzzentrum für Schwerionenforschung GmbH, 64291 Darmstadt, Germany*
[2]*Institute of Modern Physics, Chinese Academy of Science, Lanzhou 730000, China*
[3]*Instituto de Estructura de la Materia, CSIC, 28006 Madrid, Spain*
[4]*Instituto de Física, Universidad Nacional Autónoma de México, A.P. 20-364, Mexico City 01000, Mexico*
[5]*II. Physikalisches Institut, Justus-Liebig-Universität, 35392 Gießen, Germany*
[6]*Faculty of Science, University of Zagreb, 10000 Zagreb, Croatia*
[7]*CINTECX, Universidade de Vigo, E-36310 Vigo, Spain*
[8]*Faculty of Physics, University of Warsaw, 02-093 Warszawa, Poland*
[9]*Universidade de Santiago de Compostela, 15782 Santiago de Compostela, Spain*
[10]*Departamento de Ingenieria Electrica y Centro de Estudios Avanzados en Fisica, Matemáticas y Computación, Universidad de Huelva, 21071 Huelva, Spain*
[11]*Department of Atomic, Molecular and Nuclear Physics, University of Seville, 41012 Seville, Spain*
[12]*University of Edinburgh, EH1 1HT Edinburgh, United Kingdom*
[13]*Central Michigan University, Mt. Pleaseant, Michigan 48859, USA*
[14]*Flerov Laboratory of Nuclear Reactions, JINR, 141980 Dubna, Russia*
[15]*National Research Nuclear University "MEPhI", 115409 Moscow, Russia*
[16]*National Research Centre "Kurchatov Institute", Kurchatov Square 1, 123182 Moscow, Russia*
[17]*Heavy Ion Laboratory, University of Warsaw, 02-093 Warszawa, Poland*
[18]*Faculty of Physics, Warsaw University of Technology, 00-662 Warszawa, Poland*
[19]*Department of Applied Physics, University of Huelva, 21071 Huelva, Spain*
[20]*University of Huelva, 21007 Huelva, Spain*
[21]*Grand Accélérateur Nacional d'Ions Lourds–GANIL, 14076 Caen, France*
[22]*Centro de Estudios Avanzados en Física, Matemáticas y Computación (CEAFMC), Department of Integrated Sciences, University of Huelva, 21071 Huelva, Spain*
[23]*Helmholtz Research Academy Hesse for FAIR (HFHF), GSI Helmholtz Center for Heavy Ion Research, Campus Gießen, 35392 Gießen, Germany*
[24]*Faculty of Mathematics and Physics, Comenius University, 84248 Bratislava, Slovakia*
[25]*IFIN-HH, Post Office Box MG-6, Bucharest, Romania*
[26]*University of Tokyo, 113-0033 Tokyo, Japan*
[27]*Department of Physics, Chalmers University of Technology, S-41296 Göteborg, Sweden*

(Received 23 May 2024; accepted 1 August 2024; published 3 September 2024)

We report on the observation of the previously unknown isotope ^{21}Al, the first unbound aluminum isotope located beyond the proton dripline. The ^{21}Al nucleus decays by one-proton ($1p$) emission, and its in-flight decays were detected by tracking trajectories of the decay products with silicon microstrip detectors. The $1p$-emission processes were studied by analyzing the measured angular correlations of decay products ^{20}Mg $+p$. The $1p$-decay energies of the ground and low-lying excited states of ^{21}Al, its mass excess, and the proton separation energy value $S_p = -1.15^{+0.10}_{-0.07}$ MeV were determined.

DOI: 10.1103/PhysRevC.110.L031301

*Contact author: xiaodong.xu@impcas.ac.cn
†Deceased.

Motivation. Nuclear structure and decays beyond the proton drip line have been addressed in a number of experimental and theoretical studies of light isotopes; see a recent review in Ref. [1] and references therein. In particular, experimental and theoretical advances of one-proton emission have been reviewed in Ref. [2]. Based on the theoretical predictions of the separation energies and half-lives for proton unbound nuclei, one may anticipate a number of unknown unbound nuclei located within a relatively broad (by 2–5 atomic mass units) area along the proton drip line [3–5]. Beyond such a domain, i.e., toward the limits of nuclear structure, the most remote nuclear systems are expected to have only continuum spectra without resonances. Hence, they can no longer be identified as isotopes. Therefore, a new borderline indicating the limits of the existence of nuclei in the nuclear chart and the transition to chaotic-nucleon matter may be discussed [3,6].

In this work, we continue to study nuclei beyond the proton drip line using data from two experiments (S271 and S388) at the SIS facility at GSI, Germany. The present study focuses on the previously unobserved isotope ^{21}Al and reports the analysis results from both experiments.

Experiment. The experiment S271 (hereafter the first experiment) was described in detail in Refs. [7,8]. Here, a brief description of this experiment and the detector performance are provided. During this experiment, the ^{20}Mg secondary beam was produced in fragmentation of a 591 AMeV ^{24}Mg primary beam. The fragment separator (FRS) was operated in a separator-spectrometer mode, where the first half of the FRS was tuned for separation and focusing of a 450 AMeV radioactive beam of ^{20}Mg on a 2 g/cm^2 ^{9}Be secondary target in the middle focal plane (F2) of the FRS, and the second half of the FRS was set for the detection of heavy-ion (HI) decay products, e.g., ^{17}Ne. The secondary ^{20}Mg beam had a strong admixture of other ions with mass-to-charge ratios similar to ^{20}Mg. In particular, ^{21}Mg and ^{22}Al ions were transported with considerable intensities. ^{21}Al nuclei could then be produced via one-neutron removal, charge exchange and one-proton pickup of the ^{22}Al, ^{21}Mg, and ^{20}Mg projectiles, respectively. The decay products of unbound ^{21}Al nuclei were tracked using an array of double-sided silicon microstrip detectors (DSSD) located just downstream of the secondary target. The array consisted of four large-area DSSDs [9], which were employed to measure the hit coordinates of the protons and the HI decay products resulting from the in-flight decays of the studied two-proton ($2p$) precursors. The high-precision position measurements with DSSDs served for the reconstruction of all fragment trajectories, which allowed for deriving the angular HI-p and HI-p-p correlations. In the present study of ^{21}Al, the data obtained from the experiment S388 (hereafter the second experiment) using similar setup, were also analyzed. During this experiment, the ^{20,21}Mg and ^{22}Al ions were produced in fragmentation of a primary 685 AMeV ^{36}Ar beam. In particular, the 460 AMeV ^{20}Mg beam bombarded a 5 g/cm^2 thick ^{9}Be secondary target located at the F2 of the FRS. A detailed description of the second experiment can be found in Refs. [10,11].

The primary difference between the second and the first experiment is that the latter had an additional position-sensitive DSSD detector, which was placed in front of the secondary target. It measured the energy losses and hit coordinates of all secondary-beam projectiles. A two-dimensional plot of these observables is presented in Fig. 1. One may see that energy losses of Al and Mg projectiles can be discriminated, in particular events corresponding to ^{22}Al can be selected.

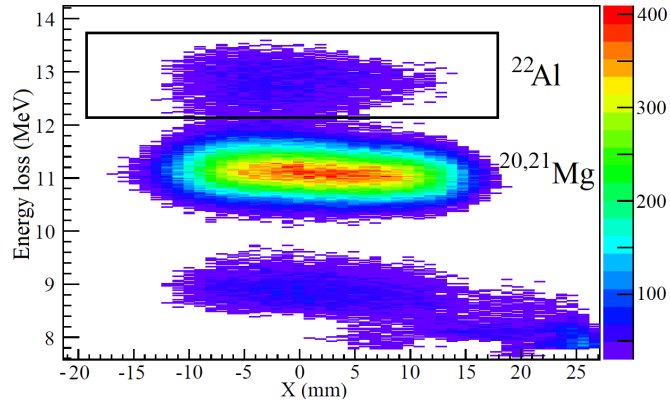

FIG. 1. Energy loss of secondary-beam ions in the DSSD located in front of the secondary ^{9}Be target as a function of their hit coordinate X (which is the transverse coordinate relative to the beam direction) during the first experiment [7,8]. Ion intensities are shown according to the scale on the right-hand side. Locations of ions of interest ^{22}Al, ^{20,21}Mg are marked. The gate for the selection of ^{22}Al projectiles is shown by a black-line rectangle.

Data. In the first experiment, the heavy-ion decay products of secondary reactions were identified utilizing their magnetic rigidity, time of flight, and energy loss. The corresponding identification plot can be found in Fig. 3 of Ref. [7]. For example, the ^{21}Al spectrum was obtained based on the angular correlations of decay products ^{20}Mg$+p$ by using their measured trajectories. With the purpose of an unambiguous interpretation, the coincidence ^{20}Mg$+p$ events were gated by choosing the Al projectiles as shown in Fig. 1, thereby suggesting a population of ^{21}Al states induced by neutron knockout reactions. In extracting the ^{21}Al spectroscopic information, we applied the same data analysis procedure and calibrations as in the $1p$-decay studies of ^{15}F, ^{18}Na, and ^{29,30}Cl [7,8,11].

In Fig. 2, we present the angular correlations between ^{21}Al decay products, namely ^{20}Mg and proton measured in the first experiment. The events in Fig. 2 were obtained by selecting only the ^{22}Al projectiles at F2 (as illustrated in Fig. 2 of Ref. [7] and Fig. 1). The respective $1p$-decay energies $E(^{20}\text{Mg}\text{-}p)$ are given by the upper axis. One can see that the low-energy part cannot be described by a two-body phase volume simulating a direct reaction with an exit channel ^{20}Mg$+p$ without any resonance in ^{21}Al. The two-body phase volume is proportional to a decay energy factor multiplied by the efficiency of detecting events ^{20}Mg$+p$. It is normalized to the measured correlations at small and large θ values ($\leqslant$40 and $\geqslant$120 mrad, respectively) where no strongly populated isolated ^{21}Al resonances are expected. Due to such normalization, the two-body phase-volume component is considered as an upper-limit estimate of the possible contribution of the nonresonant branch into the measured correlations. One can see two peaks exceeding the estimated background, which are

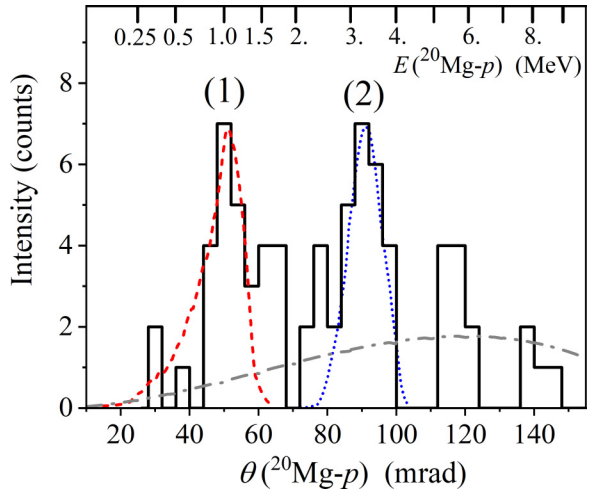

FIG. 2. Angular $\theta(^{20}\text{Mg}\text{-}p)$ correlations derived from the measured $^{20}\text{Mg}+p$ coincidences obtained in the first experiment (histogram). The ^{22}Al projectiles before the secondary target were selected. The respective $1p$-decay energies $E(^{20}\text{Mg}\text{-}p)$ are given by the upper axis. The peaks (1) and (2) were reproduced by applying Monte-Carlo simulations of $1p$ decays of two ^{21}Al states into the ^{20}Mg g.s. (shown by the dashed and dotted curves) with the evaluated $1p$-decay energies of $1.15^{+0.10}_{-0.07}$ and $3.15^{+0.15}_{-0.12}$ MeV, respectively. The dash-dotted curve is the upper-limit estimate of a nonresonance background by using phase-volume simulations.

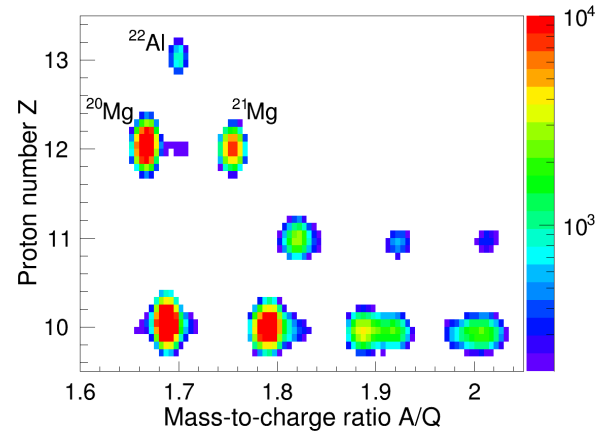

FIG. 3. Two-dimensional identification plot of Z vs A/Q for the heavy ions detected at the FRS during the second experiment with the ^{20}Mg - ^{17}Ne setting. Projectiles of interest ^{21}Mg and ^{22}Al were also produced and transported as byproducts with reasonable intensities. Ion intensities are shown according to the logarithmic scale on the right-hand side.

labeled as (1) and (2) in Fig. 2. They indicate the population and $1p$ decays of two low-energy states in ^{21}Al.

To determine the decay energies Q_{1p} corresponding to the peaks exhibited in Fig. 2, we performed Monte Carlo simulations of the detector response to the $1p$ decays of ^{21}Al states by using the GEANT software [12], which was described in detail in Refs. [7,8]. The simulations were computed independently for peaks (1) and (2). For each peak, a number of simulations of angular $\theta(^{20}\text{Mg}\text{-}p)$ correlations with varied $1p$-decay energies were performed. The intrinsic width of every ^{21}Al state was assumed to be very small, i.e., 1 keV. Then every simulated spectrum was compared with the data around the peaks (1) or (2) by using the standard Kolmogorov test, which computes the probability that the simulated $\theta(^{20}\text{Mg}\text{-}p)$ spectrum matches the respective experimental pattern [13]. According to the Kolmogorov test, two compared histograms are statistical variations of the same distribution if the Kolmogorov-test probability value is larger than 0.5. The Q_{1p} values were derived from the distributions of the calculated probabilities with the corresponding uncertainty. Consequently, the Q_{1p} values were determined to be $1.15^{+0.10}_{-0.07}$ and $3.15^{+0.15}_{-0.12}$ MeV, which corresponds to descriptions of the peaks (1) and (2) in Fig. 2 with probabilities of 0.94 and 0.80, respectively.

In order to verify the states observed in the first experiment, we analyzed the data obtained during one setting of the second experiment, in which reactions with a ^{20}Mg secondary beam producing the known ^{19}Mg were employed for reference purposes [10]. In this measurement, the first half of the FRS was optimized to transport the ^{20}Mg beam, and the second half of the FRS was tuned to transmit the ^{17}Ne ions. Figure 3 shows the particle identification plot for the ions that reached the last focal plane of the FRS (F4), where the ions' proton number Z versus their mass-to-charge ratio A/Q ($Q = Z$ in our case of light ions and high energy) are shown. One may see that ^{20}Mg ions were also transported down to F4 because their A/Q ratio is similar to that of ^{17}Ne. Other ions of interest, such as ^{21}Mg and ^{22}Al, were also produced and transported through the FRS with the signal-to-background ratio larger than 100.

The Fig. 4 displays the $\theta(^{20}\text{Mg}\text{-}p)$ spectra obtained from the $^{20}\text{Mg}+p$ coincidences measured in the second experiment. Two peaks are also present, which suggests the similar $1p$ decays of low-energy states in ^{21}Al. Since there was no

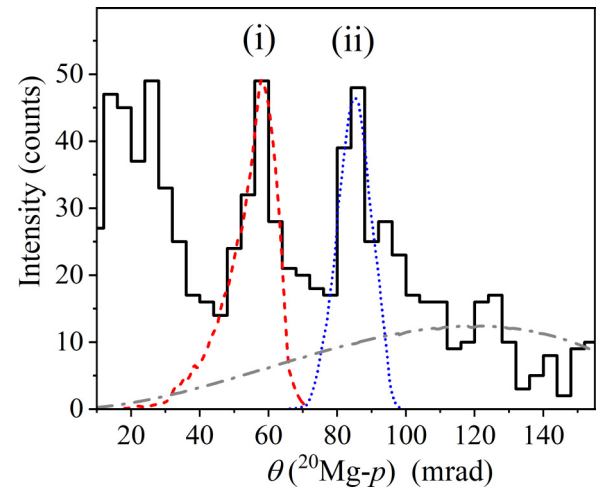

FIG. 4. Angular $\theta(^{20}\text{Mg}\text{-}p)$ correlations derived from the measured $^{20}\text{Mg}+p$ coincidences obtained in the second experiment (histogram). The contributions of all secondary-beam ions illustrated in Fig. 3 are included. The dashed and dotted curves representing the Monte Carlo simulations of $1p$ decays of two ^{21}Al states into the ^{20}Mg g.s. are displayed for illustration purposes. The nonresonance background (dash-dotted curve) is estimated by using two-body phase-volume simulations.

selection of incoming ions before the secondary target, the ^{21}Al isotope may be produced in reactions of one-neutron knockout, charge exchange, and one-proton pickup of the ^{22}Al, ^{21}Mg, and ^{20}Mg projectiles, respectively. In comparison with the data shown in Fig. 2, the distribution exhibits a similar shape characterized by two peaks centered around 60 and 90 mrad, accompanied by a broad distribution at smaller $\theta(^{20}\text{Mg}\text{-}p)$ values. The peaks repeat the corresponding structures in Fig. 2 though the angular resolution is worse. For illustration purposes, the simulations similar to those in Fig. 2 are added, though the corresponding $1p$-decay energies cannot be derived accurately because of the ambiguous momenta of projectiles at F2 in this case.

The comparison of the results of Monte Carlo simulations of two experiments demonstrates a reasonable agreement between the simulated 90-mrad peaks in Fig. 4 and in Fig. 2 with the derived Q_{1p} value of $3.15^{+0.15}_{-0.12}$ MeV. Both peaks have full width at half maximum (FWHM) values of ≈1.0 MeV. There is also a qualitative agreement, with an insignificant deviation in the positions of the 50-mrad peaks. The data of the first experiment have smaller statistics, but their interpretation is straightforward because of the dominating secondary reaction $^{22}\text{Al} \rightarrow {}^{21}\text{Al} + n$. Therefore, we assign the ^{21}Al g.s. to the 50-mrad peak in Fig. 2 with the derived $1p$-decay energy of $1.15^{+0.10}_{-0.07}$ MeV. The FWHM value of the peak (1) in Fig. 2 is ≈0.5 MeV. The corresponding estimate of the ^{21}Al g.s. width derived by simulations of these peaks provides only the upper-limit value $\Gamma_{\text{g.s.}} < 400$ keV, which is mainly due to the experimental resolution.

The obtained distributions of vertices of the measured $^{20}\text{Mg} + p$ trajectories allow for deriving the half-life values (and therefore widths) of ^{21}Al states. We estimated the half-lives of the observed ^{21}Al levels by measuring the distributions of their decay vertices in the same way as in the previous study of $2p$ decay of ^{30}Ar [14]. All vertex distributions are located within the reaction target, and therefore we found no indication of long-lived states in ^{21}Al, which results in the assignment of an upper limit of the half-life of 10 ps. According to the energy-time uncertainty relation, the corresponding lower-limit estimate of state widths in ^{21}Al is $\approx 5 \times 10^{-8}$ keV.

Discussion. The assigned levels and decay scheme of ^{21}Al derived from the observed angular correlations are shown in Fig. 5. The g.s. of ^{21}Al is unbound with the $1p$-decay energy of $1.15^{+0.10}_{-0.07}$ MeV. The mass of ^{21}Al can be derived by using the masses of ^{20}Mg and proton together with the Q_{1p} value, which then can be compared with available theoretical predictions. The AME2020 atomic mass evaluation [15] predicts that mass excess (M.E.) of the ^{21}Al g.s. is 27.1(6) MeV, which exceeds the measured M.E. value of 25.95(10) MeV by 1.15 MeV. Such a difference with the AME2020 predictions calls for an update of the the mass extrapolation method used in the AME2020 evaluation. The $1p$-unbound nuclei may be described by the empirical S_p systematics of $1p$-emitting $d_{5/2}$ states in light nuclei. The systematics is based on a parametrization of a mirror energy difference (MED) [16] by using the available experimental data on neutron-rich nuclei. The MED definition is $\text{MED} = S_n - S_p$ (here S_n and S_p are

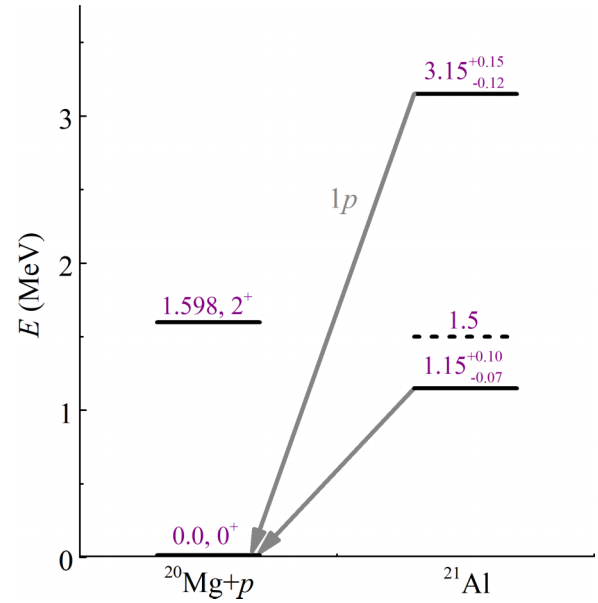

FIG. 5. Proposed decay scheme of two low-energy states observed in ^{21}Al with assigned $1p$-decay channels to the known ^{20}Mg ground state, whose energies are given relative to the $1p$ threshold. The dashed line at 1.5 MeV shows the tentative position of the first excited state indicated in the data in Fig. 2.

$1n$ and $1p$ separation energies in mirror states of neutron- and proton-rich nuclei, respectively), and its parametrization is $\text{MED} = (Z/A^{1/3})\text{MED}'$, where the MED′ value does not depend on the proton number Z and mass number A [16]. This parametrization predicts $S_p = -1.315$ MeV for ^{21}Al (by using the S_n value of its mirror partner $^{21}\text{O}_{\text{g.s.}}(5/2^+)$ and the corresponding MED value [16]), which is in reasonable agreement with the measured S_p value of $-1.15^{+0.10}_{-0.07}$ MeV. The mass of the ^{21}Al g.s. was also predicted by the systematics proposed for the mass differences of mirror nuclei (the improved Kelson-Garvey mass relations [17]). The estimated value $S_p = -1.265(13)$ MeV roughly agrees with the data within the reported uncertainties.

There are several theoretical predictions of the low-energy states and their widths dedicated to ^{21}Al, e.g. Refs. [18–22]. Let us consider the predictions calculated by using both the microscopic cluster model and potential model [18]. The mirror symmetry between the widths of low-lying resonance states and the asymptotic normalization coefficients of their mirror analogs was employed. The potential model used the same potential well parameters obtained from descriptions of the respective mirror states in ^{21}O, which are known experimentally. The predicted $1p$-decay energies and widths (E_{1p}, Γ) of the lowest ^{21}Al states with $d_{5/2}$, $s_{1/2}$, and $d_{3/2}$ $1p$-configurations are (1.21 MeV, 0.7 keV), (1.55 MeV, 248 keV), and (2.63 MeV, $\lessapprox$0.08 keV), respectively [18]. The calculated $d_{5/2}$-state energy is close to the measured value of the ^{21}Al g.s., but the corresponding width is too small to be obtained with our setup, which is able to measure the predicted width of the first-excited $s_{1/2}$ state in a future dedicated experiment. One should note that states in ^{21}Al with core $^{20}\text{Mg}^*(2^+)$ excitations (predicted by the microscopic cluster

model in Ref. [18]) were not identified in the present work as their identification requires the additional detection of γ rays from the fragments ^{20}Mg*.

For illustration purposes, the low-lying states in ^{21}Al with $d_{5/2}$, $s_{1/2}$, and $d_{3/2}$ $1p$-configurations were also calculated by using a nuclear-potential model applied in Ref. [3] in a manner similar to Ref. [18]. The potential parameters were first fixed by reproducing the known lowest states in the mirror ^{21}O nucleus, in particular the energy of the $s_{1/2}$ $1/2^+$ state located 1220 keV above the $5/2^+$ g.s. In Fig. 6(a), the calculated root-mean-squared radii $r_{\rm rms}$ of these bound states are shown. One may see a large spatial difference between the s and d $1n$-configurations. Then the same configuration states in the mirror unbound nucleus ^{21}Al should be displaced differently by Coulomb repulsion which illustrates the effect of the Thomas-Ehrman shift [23,24]. The latter is often observed in $1p$-unbound nuclei with s and d configurations as a reduced energy between the respective $1p$ states. The calculated level energies in ^{21}Al as functions of nuclear radius are presented in Fig. 6(b), where the trend of decreasing level energies as the radius increases demonstrates the effect of the decreased Coulomb repulsion. The energies of states with $5/2^+$ and $3/2^+$ configurations match the measured energies of 1.15 and 3.15 MeV derived from the peaks in Fig. 2, respectively. According to the level-energy predictions shown in Fig. 6(b), the energy of the $1/2^+$ state with $s_{1/2}$ $1p$-configuration is expected only ≈0.4 MeV above the $5/2^+$ g.s. of ^{21}Al, which is ≈820 keV less than the energy difference in the bound mirror ^{21}O nucleus.

The excitation energy of the first excited state ($1/2^+$) in ^{21}Al was also calculated within the many-body perturbation theory [19] and the Gamow shell-model [20], which is in agreement with the value provided by the applied potential model. Such a relatively small energy difference between the ground state and the first excited state indicates that the low-energy peak (within the range of 45–65 mrad) in Fig. 4 may consist of the $5/2^+$ and $1/2^+$ states which were unresolved due to the limited energy resolution. In Fig. 2, there is an indication of a possible population of the first excited state at ≈1.5 MeV, for which the unexplained part of the angular $\theta(^{20}\mathrm{Mg}\text{-}p)$ distribution points at ≈65 mrad.

It is also worth noting that the spectrum of ^{21}O, which is the mirror nucleus of ^{21}Al, exhibits several low-energy levels with excitation energy below the one-neutron threshold of 3.8 MeV. Considering the mirror symmetry, more low-energy states in ^{21}Al may be found. For example, an indication of possible excitations in ^{21}Al can be spotted in Fig. 2 in the region of 5–6 MeV (i.e., within the range of 110–120 mrad). Though the mentioned regions do not have sufficient statistics for a quantitative investigation, future experiments with higher statistics and better resolution will resolve these questions.

Conclusion. The first spectroscopy of the previously unknown isotope ^{21}Al, which decays via $1p$ emission, revealed two low-energy states, which are tentatively assigned as ($5/2^+$) ground state and ($3/2^+$) excited state. The first-excited $1/2^+$ state, which is predicted at an energy of 0.3–0.4 MeV above the g.s., was not identified yet, though its population is not excluded in the experimental angular-correlation pattern in Fig. 2. The mass excess of the ^{21}Al g.s. was derived from the measured Q_{1p} value to be +25.95(10) MeV, which is a challenging test for the predictions by nuclear mass models.

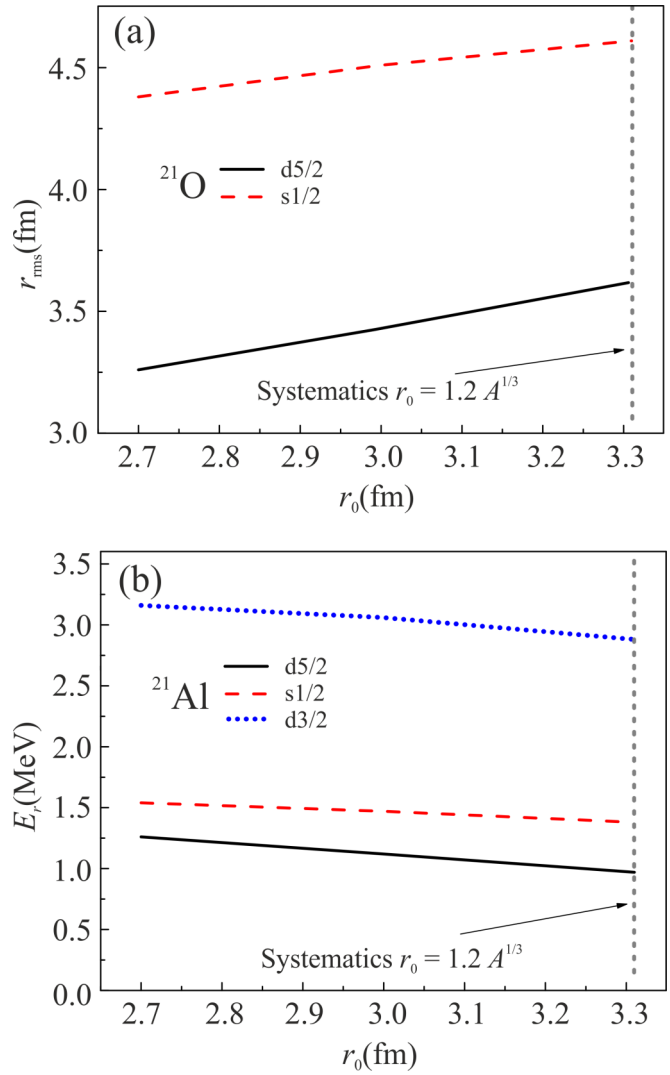

FIG. 6. (a) The potential model [3] calculations of root-mean-square radii r_{rms} of the $s_{1/2}$ and $d_{5/2}$ $1n$-configurations in the bound ^{21}O nucleus (the dashed and solid curves, respectively) as functions of nuclear radius r_0. The large spatial difference of the s and d configurations results in a large Thomas-Ehrman shift between the respective configurations in the mirror unbound nucleus ^{21}Al. (b) Energies E_r of the lowest states in unbound ^{21}Al with $s_{1/2}$, $d_{5/2}$, and $d_{3/2}$ $1p$-configurations (the dashed, solid, and dotted curves, respectively) as functions of r_0. The E_r values were calculated relative to the ^{20}Mg $+p$ threshold by applying the same model. The vertical dotted line in both panels show the radius obtained from the systematic estimate $r_0 = 1.2 \times A^{1/3}$.

The observation of unbound ^{21}Al g.s. leads to the following statements about its neighboring nuclei in the nuclear chart: (1) Together with the very recent mass measurement of ^{22}Al which provides its $1p$-separation energy of about 100 keV [25,26], one may conclude that the proton drip line

is established in the Al isotopic chain. (2) The loosely bound isotope ^{22}Si (recent mass measurement for this nucleus proves that it is bound [27]) is a two-proton Borromean nucleus whose three-body configuration $^{20}\mathrm{Mg}+p+p$ has no bound sub-system $^{20}\mathrm{Mg}+p \rightarrow {}^{21}\mathrm{Al}$.

Acknowledgments. This work was supported in part by the Helmholtz International Center for FAIR (HIC for FAIR); the Helmholtz Association (Grant No. IK-RU-002); the European Union's Horizon Europe Research and Innovation program under Grant Agreement No. 101057511 (EURO-LABS); the Chinese Academy of Sciences President's International Fellowship Initiative (Grant No. 2024PVA0005); the Russian Science Foundation (Grant No. 22-12-00054); the Polish National Science Center (Contract No. 2019/33/B/ST2/02908); the Helmholtz-CAS Joint Research Group (Grant No. HCJRG-108); the Ministry of Education & Science, Spain (Contract No. FPA2016-77689-C2-1-R); the Ministry of Economy, Spain (Grant No. FPA2015-69640-C2-2-P); the Hessian Ministry for Science and Art (HMWK) through the LOEWE funding scheme; the Justus-Liebig-Universität Giessen (JLU) and the GSI under the JLU-GSI strategic Helmholtz partnership agreement; and DGAPA-PAPIIT IG101423. This work was carried out in the framework of the Super-FRS Experiment Collaboration.

[1] M. Pfützner, I. Mukha, and S. M. Wang, Prog. Part. Nucl. Phys. **132**, 104050 (2023).
[2] M. Pfützner, M. Karny, L. V. Grigorenko, and K. Riisager, Rev. Mod. Phys. **84**, 567 (2012).
[3] L. V. Grigorenko, I. Mukha, D. Kostyleva, C. Scheidenberger, L. Acosta, E. Casarejos, V. Chudoba, A. A. Ciemny, W. Dominik, J. A. Dueñas *et al.*, Phys. Rev. C **98**, 064309 (2018).
[4] L. Neufcourt, Y. Cao, S. Giuliani, W. Nazarewicz, E. Olsen, and O. B. Tarasov, Phys. Rev. C **101**, 014319 (2020).
[5] M. Gonçalves, N. Teruya, O. A. P. Tavares, and S. B. Duarte, Phys. Lett. B **774**, 14 (2017).
[6] D. Kostyleva, I. Mukha, L. Acosta, E. Casarejos, V. Chudoba, A. A. Ciemny, W. Dominik, J. A. Dueñas, V. Dunin, J. M. Espino *et al.*, Phys. Rev. Lett. **123**, 092502 (2019).
[7] I. Mukha, K. Sümmerer, L. Acosta, M. A. G. Alvarez, E. Casarejos, A. Chatillon, D. Cortina-Gil, I. A. Egorova, J. M. Espino, A. Fomichev *et al.*, Phys. Rev. C **82**, 054315 (2010).
[8] I. Mukha, L. Grigorenko, L. Acosta, M. A. G. Alvarez, E. Casarejos, A. Chatillon, D. Cortina-Gil, J. M. Espino, A. Fomichev, J. E. García-Ramos *et al.*, Phys. Rev. C **85**, 044325 (2012).
[9] M. Stanoiu, K. Sümmerer, I. Mukha, A. Chatillon, E. Cortina Gil, M. Heil, J. Hoffman, O. A. Kiselev, N. Kurz, and W. Ott (S271 Collaboration), Nucl. Instrum. Methods Phys. Res., Sect. B **266**, 4625 (2008).
[10] X.-D. Xu, I. Mukha, L. V. Grigorenko, C. Scheidenberger, L. Acosta, E. Casarejos, V. Chudoba, A. A. Ciemny, W. Dominik, J. Duénas-Díaz *et al.*, Phys. Rev. C **97**, 034305 (2018).
[11] I. Mukha, L. V. Grigorenko, D. Kostyleva, L. Acosta, E. Casarejos, A. A. Ciemny, W. Dominik, J. A. Dueñas, V. Dunin, J. M. Espino *et al.*, Phys. Rev. C **98**, 064308 (2018).
[12] GEANT detector simulation tool, CERN software library.
[13] W. T. Eadie *et al.*, *Statistical Methods in Experimental Physics* (North-Holland, Amsterdam, 1971).
[14] I. Mukha, L. V. Grigorenko, X. Xu, L. Acosta, E. Casarejos, A. A. Ciemny, W. Dominik, J. Duénas-Díaz, V. Dunin, J. M. Espino *et al.*, Phys. Rev. Lett. **115**, 202501 (2015).
[15] M. Wang, W. J. Huang, F. G. Kondev, G. Audi, and S. Naimi, Chin. Phys. C **45**, 030003 (2021).
[16] H. T. Fortune, Phys. Rev. C **97**, 034301 (2018).
[17] J. Tian, N. Wang, C. Li, and J. Li, Phys. Rev. C **87**, 014313 (2013).
[18] N. K. Timofeyuk, B. Fernández-Domínguez, P. Descouvemont, W. N. Catford, F. Delaunay, and J. S. Thomas, Phys. Rev. C **86**, 034305 (2012).
[19] J. D. Holt, J. Menéndez, and A. Schwenk, Phys. Rev. Lett. **110**, 022502 (2013).
[20] N. Michel, J. G. Li, F. R. Xu, and W. Zuo, Phys. Rev. C **100**, 064303 (2019).
[21] C. Ma, Y. Y. Zong, S. Q. Zhang, J. Li, K. Wang, Y. M. Zhao, and A. Arima, Phys. Rev. C **103**, 054326 (2021).
[22] H. H. Li, Q. Yuan, J. G. Li, M. R. Xie, S. Zhang, Y. H. Zhang, X. X. Xu, N. Michel, F. R. Xu, and W. Zuo, Phys. Rev. C **107**, 014302 (2023).
[23] R. G. Thomas, Phys. Rev. **88**, 1109 (1952).
[24] J. B. Ehrman, Phys. Rev. **81**, 412 (1951).
[25] M. Sun, Y. Yu, X. Wang, M. Wang, J. Li, Y. Zhang, K. Blaum, Z. Chen, R. Chen, H. Deng *et al.*, Chin. Phys. C **48**, 034002 (2024).
[26] S. E. Campbell, G. Bollen, B. A. Brown, A. Dockery, C. M. Ireland, K. Minamisono, D. Puentes, B. J. Rickey, R. Ringle, I. T. Yandow *et al.*, Phys. Rev. Lett. **132**, 152501 (2024).
[27] Y. Zhang (private communication).